

• Original Paper •

Statistical Modeling with a Hidden Markov Tree and High-resolution Interpolation for Spaceborne Radar Reflectivity in the Wavelet Domain

Leilei KOU¹, Yinfeng JIANG², Aijun CHEN¹, and Zhenhui WANG¹

¹Key Laboratory of Meteorological Disaster, Ministry of Education/Joint International Research Laboratory of Climate and Environment Change/Collaborative Innovation Center on Forecast and Evaluation of Meteorological Disasters, Nanjing University of Information Science & Technology, Nanjing 210044, China

²Nanjing University of Information Science & Technology, Nanjing 210044, China

(Received 25 February 2020; revised 21 July 2020; accepted 20 August 2020)

ABSTRACT

With the increasing availability of precipitation radar data from space, enhancement of the resolution of spaceborne precipitation observations is important, particularly for hazard prediction and climate modeling at local scales relevant to extreme precipitation intensities and gradients. In this paper, the statistical characteristics of radar precipitation reflectivity data are studied and modeled using a hidden Markov tree (HMT) in the wavelet domain. Then, a high-resolution interpolation algorithm is proposed for spaceborne radar reflectivity using the HMT model as prior information. Owing to the small and transient storm elements embedded in the larger and slowly varying elements, the radar precipitation data exhibit distinct multiscale statistical properties, including a non-Gaussian structure and scale-to-scale dependency. An HMT model can capture well the statistical properties of radar precipitation, where the wavelet coefficients in each sub-band are characterized as a Gaussian mixture model (GMM), and the wavelet coefficients from the coarse scale to fine scale are described using a multiscale Markov process. The state probabilities of the GMM are determined using the expectation maximization method, and other parameters, for instance, the variance decay parameters in the HMT model are learned and estimated from high-resolution ground radar reflectivity images. Using the prior model, the wavelet coefficients at finer scales are estimated using local Wiener filtering. The interpolation algorithm is validated using data from the precipitation radar onboard the Tropical Rainfall Measurement Mission satellite, and the reconstructed results are found to be able to enhance the spatial resolution while optimally reproducing the local extremes and gradients.

Key words: spaceborne precipitation radar, hidden Markov tree model, Gaussian mixture model, interpolation in the wavelet domain, multiscale statistical properties

Citation: Kou, L. L., Y. F. Jiang, A. J. Chen, and Z. H. Wang, 2020: Statistical modeling with a hidden Markov tree and high-resolution interpolation for spaceborne radar reflectivity in the wavelet domain. *Adv. Atmos. Sci.*, **37**(12), 1359–1374, <https://doi.org/10.1007/s00376-020-0035-5>.

Article Highlights:

- The HMT model can capture multiscale statistics of radar reflectivity, including a non-Gaussian structure and interscale dependency.
- The variance decay and multiscale processes controlling parameters in the HMT model can be estimated from ground radar reflectivity images.
- Wavelet-based interpolation with the HMT model as prior information can recover small-scale features of spaceborne radar reflectivity data.

1. Introduction

Precipitation is a key component of the water cycle,

and observations of precipitation have played a key role in meteorology and hydrology (Sorooshian et al., 2011). Global precipitation measurement with high spatiotemporal resolution is important for various applications, including water resource management, numerical weather prediction, climate modeling at local scales, and flash flood forecasting (Wang and Wolff, 2009; Prakash et al., 2016; Skofronick-

* Corresponding author: Leilei KOU
Email: cassie320@163.com

Jackson et al., 2017; Kou et al., 2018). The precipitation radar (PR) onboard the Tropical Rainfall Measuring Mission (TRMM) satellite was the first space-based weather radar, and the availability of spaceborne PR data has been highly beneficial for observations of precipitation (Kozu et al., 2001). Following the success of the TRMM satellite, the Global Precipitation Measurement (GPM) core satellite was launched in February 2014 and started its observations (Hou et al., 2014). A constellation of nine satellites for the GPM mission promises to provide observations of high precision precipitation and cloud dynamics at a global scale with a 3-h revisiting time, which creates opportunities for improving climate modeling and disaster prediction at local scales. Spaceborne radar is vital for global precipitation measurements, particularly for regions in which high-resolution ground radars (GRs) are absent, or in mountainous regions where radar blockage is a severe problem (Kozu et al., 2001; Ebtehaj et al., 2012; Skofronick-Jackson et al., 2017). However, the low horizontal resolution ($4 \text{ km} \times 4 \text{ km}$ or $5 \text{ km} \times 5 \text{ km}$) of spaceborne radars limits their use for small-scale precipitation observation applications such as disaster prediction and warning, as well as detailed information on extremes that could be used in a data assimilation setting or in climate modeling. Therefore, obtaining high-resolution data on the small-scale variability of precipitation from space continues to present a challenge both in a theoretical and practical sense.

Interpolation is a widely used method for increasing the data resolution in order to obtain more detailed information (Gonzalez and Woods, 2007; Demirel and Anbarjafari, 2011; Azam et al., 2014; Chavez-Roman and Ponomaryov, 2014). Conventional data interpolation methods, such as linear, bicubic, or Cressman interpolation, are the most common spatial domain interpolation methods of weather radar data and have the advantage of high speed but suffer from staircase effects and blurring due to the band limit constraints. A number of methods have been proposed to overcome the shortcomings of these spatial domain interpolation methods based on low-pass filtering (Deidda, 2000; Tao and Barros, 2010; Chavez-Roman and Ponomaryov, 2014; Ruzanski and Chandrasekar, 2015; Jiao et al., 2016). Jiao et al. (2016) proposed an interpolation method for weather radar data based on Fourier spectrum analysis. Ruzanski and Chandrasekar (2015) performed temporal interpolation of meteorological radar data using a kernel-based Lagrangian nowcasting technique with a fast Fourier transform. Tao et al. (2010) used fractal interpolation to enhance the resolution of satellite precipitation products based on iterated function systems and fractal Brownian surfaces. However, the key geometrical and statistical properties of radar precipitation observations have not been explored or included in spatial interpolation algorithms.

The spatial and temporal variabilities of precipitation exhibit distinct statistical space-time structures at multiple scales (Perica and Foufoula-Georgiou, 1996; Harris et al., 2001; Ebtehaj and Foufoula-Georgiou, 2011). Such multiscale statistical characteristics have been studied using

several approaches in the frequency and wavelet domain, such as the theory of multifractals, multiplicative cascades, exponential Langevin-type models, and the cascades of Gaussian-scale mixtures (Badas et al., 2006; Deidda et al., 2006; Gupta et al., 2006; Venugopal et al., 2006; Sapozhnikov and Foufoula-Georgiou, 2007; Ebtehaj and Foufoula-Georgiou, 2011). These multiscale representations have proven to be useful for quantifying the precipitation variability at multiple scales and can be exploited as prior information. In view of the sparseness of precipitation in the wavelet domain, Ebtehaj et al. (Ebtehaj et al., 2012; Ebtehaj and Foufoula-Georgiou, 2013) recast precipitation downscaling into an ill-posed inverse problem and estimated the high-resolution information with regularization. Based on the non-Gaussian and local coherent structure of radar reflectivity data in the wavelet domain, Kou et al. (2019) proposed an interpolation algorithm for radar reflectivity data using the Gaussian-scale mixtures model.

Small-scale variability is important for accurate prediction and warning of heavy precipitation. In this study, the multiscale statistical characteristics of radar reflectivity data are studied and modeled using a hidden Markov tree (HMT) in the wavelet domain. A high-resolution interpolation algorithm for spaceborne radar reflectivity based on the HMT model is proposed to enhance the resolution and reproduce the small-scale detailed information. First, the characteristics of the thicker-than-Gaussian structure and interscale dependency of the radar reflectivity data are studied, and these characteristics are matched using the HMT model. Then, the variance decay and multiscale processes controlling parameters across different scales in the HMT model are learned and estimated from a set of matched high-resolution GR reflectivity images dominated by convective precipitation. Furthermore, a Wiener filter is applied locally to each sub-band to obtain the fine-scale coefficients. Finally, high-resolution satellite reflectivity data are generated with an inverse wavelet transform. Case studies are conducted for the proposed method to prove that it can capture and reproduce the small-scale details of the spatial distribution of precipitation, such as sharp variations and extreme values.

2. HMT modeling for radar reflectivity

2.1. Statistical characteristics of modeling in the wavelet domain

Because of the high precipitation intensity embedded in the lower intensity regions, large gradients and discontinuities are present in precipitation echoes. In other words, the probability distribution of the precipitation reflectivity in the derivative space (e.g., the wavelet domain) has a large mass around zero (nearby pixels with similar values) and a few heavy values (steep gradients), thereby representing a heavy-tailed non-Gaussian distribution. In addition, the evolution of precipitation from coarse to fine scale often displays self-similarity, which can be considered as a self-similar mul-

tifractal process (Deidda, 2000; Deidda et al., 2006). Prior information about these multiscale statistics of precipitation is important for reproducing the desired properties of precipitation fields.

For remotely sensed precipitation data obtained by ground or spaceborne radar, some common statistical properties and mathematical signatures exist that can be characterized and exploited for precipitation modeling and further applications (Ebtehaj and Foufoula-Georgiou, 2011; Foufoula-Georgiou et al., 2014). The wavelet transform using a multiresolution analysis framework can represent well the multiscale processes of precipitation, and it is useful for quantifying the rainfall variability at multiple scales (Willsky, 2002; Azam et al., 2014). With prior modeling of wavelet coefficients of radar reflectivity data, the estimated finer wavelet coefficients can effectively recover the essential properties of the reflectivity data.

Before studying the statistical characteristics of the radar reflectivity data, the data from the TRMM PR and the GR were quality controlled and spatiotemporally matched. The level II algorithm of the TRMM PR profile (2A25) was used, which includes ground clutter filtering, attenuation and beam filling correction (Kozu et al., 2001). The GR data from the ground Doppler radar at Longwang Mountain (32.1908°N, 118.6969°E) in Nanjing city, China, were processed with anomalous propagations and ground clutter removal using the NCAR SOLO II algorithm. Using the results in Zhu et al. (2016) that employed 245 TRMM PR and Nanjing GR matchup cases to determine the calibration biases, the system calibration bias of the Nanjing GR was corrected by adding a bias adjustment. The temporal matching was carried out with a 6-min window centered on the TRMM PR overpass time. The spatial matchup scheme was based on the grid matching method (Liao and Meneghini, 2009), in which both sets of data were interpolated to a common 3D Cartesian coordinate system. The gridded GR data were interpolated from the GR spherical coordinate system centered at the GR using a cubic linear interpolation algorithm, with a vertical resolution of about 1 km to a height of 20 km and a horizontal resolution of about 1 km to a horizontal extent of ± 150 km. The TRMM PR data were also resampled into Cartesian coordinates with a horizontal resolution of 4 km, and the displacement of the PR samples was corrected as well (Wang and Wolff, 2009; Kou et al., 2018).

After data preprocessing, the statistical characteristics of the high-resolution radar reflectivity data, including non-Gaussian marginal statistics and scale-to-scale dependency, were first studied with convective precipitation cases. Then, the intrascale and interscale statistical characteristics of the reflectivity data were matched using the HMT model. In the wavelet domain of the HMT model, the distribution densities of the wavelet coefficients were approximated by a Gaussian mixture model (GMM), and the dependencies of multiscale wavelet coefficients were represented by a Markov process and state transition parameters (Crouse et al., 1998; Romberg et al., 2001; Li et al., 2010).

The radar data used in this paper are the reflectivity at a height of 3 km in Cartesian coordinates, and a shift-invariant undecimated orthogonal wavelet transform and Haar wavelet were used for wavelet decomposition (Nason and Silverman, 1995). Figure 1a shows the spaceborne radar reflectivity image at 3 km height from TRMM PR at 0456:41 UTC 27 May 2008, and Fig. 1b shows the coincidental high-resolution GR CAPPI (Constant Altitude Plan Position Indicator) at 0459:00 UTC. Figure 1c shows the marginal probability distribution on the log scale of the wavelet coefficient in the horizontal sub-band of the image presented in Fig. 1b, and Fig. 1d is the corresponding statistical histogram of the horizontal wavelet coefficient. It can be seen from Fig. 1d that the wavelet coefficient of the precipitation image has heavy tail that is significantly thicker than those of a Gaussian distribution; this usually corresponds to the heavy precipitation gradients and intensities.

Figure 2 shows another convective precipitation image obtained by the Nanjing GR at 0530:00 15 August 2010. Figure 2b shows the wavelet coefficients in the horizontal band of the radar reflectivity data presented in Fig. 2a, and Fig. 2c is the corresponding probability distribution of the wavelet coefficients, where the asterisk denotes the histogram. It can be seen that the histogram is also significantly different from a Gaussian distribution, with much heavier tails than those of a Gaussian function.

This heavy-tail property implies that most wavelet coefficients contain very little information, while a few wavelet coefficients represent significant information. The Gaussian mixture distribution can be employed to characterize the non-Gaussian marginal statistics and the heavy-tail properties of the radar reflectivity:

$$f(w_i) = \sum_{m=1}^M P_{s_i}(m) f_{w_i|s_i}(w_i|s_i = m) , \quad (1)$$

where s_i is the state m of the i th coefficient w_i , and $P_{s_i}(m)$ represents the probability that the wavelet coefficient w_i belongs to the state m ; $f_{w_i|s_i}(w_i|s_i = m)$ is the Gaussian conditional probability distribution function (PDF). Figure 3 shows the two-state, zero-mean mixture model by the PDF of the state variable s ($s = 0$ or 1), and the variances of the Gaussian PDF corresponding to each state. For $M = 2$, each state is modeled as one of two states: “1” represents the “high” state corresponding to a wavelet atom with high variance and significant signal energy, and “0” denotes the “low” state corresponding to a wavelet atom with low variance and little signal information. The results shown in Fig. 3 correspond to a two-state GMM. In the GMM, the value of the coefficient w is observed, but the value of the state variable s is hidden, which should be estimated.

The black solid line in Fig. 1d is the fitted two-state GMM distribution (on the log scale) obtained using the expectation maximization (EM) algorithm (Figueiredo and Nowak, 2003), where the asterisks denote the original probability distribution of wavelet coefficients. The fitted GMM dis-

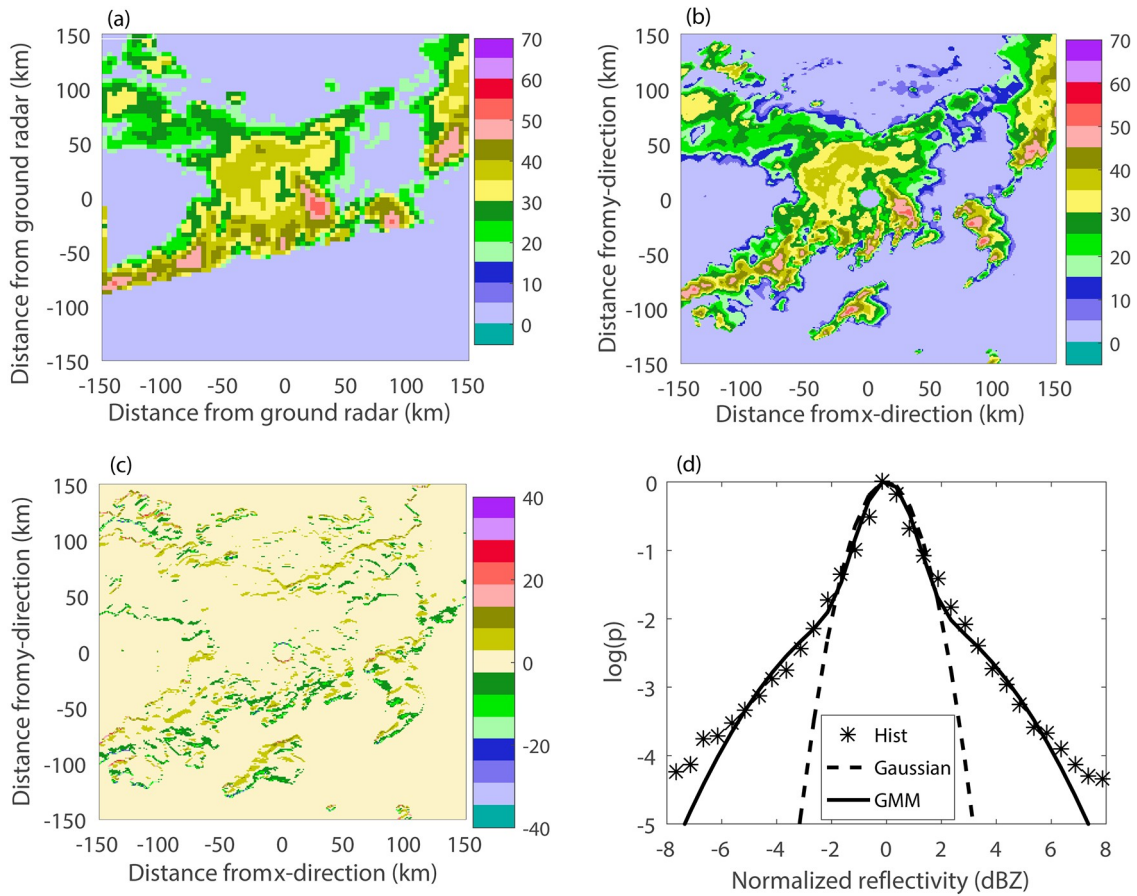


Fig. 1. (a) Radar reflectivity image from TRMM PR obtained at 0456:41 UTC 27 May 2008, (b) the coincidental reflectivity image captured by the GR in Nanjing at 0459:00 UTC, (c) wavelet coefficients in the horizontal sub-band of the reflectivity image in (b), and (d) the corresponding log histogram (asterisks) of the wavelet coefficients normalized by the standard deviation. A heavier tail than the Gaussian distribution [dotted line in (d)] is clear in the precipitation reflectivity image in the wavelet domain, and the solid line in (d) is the fitted GMM distribution with the EM algorithm.

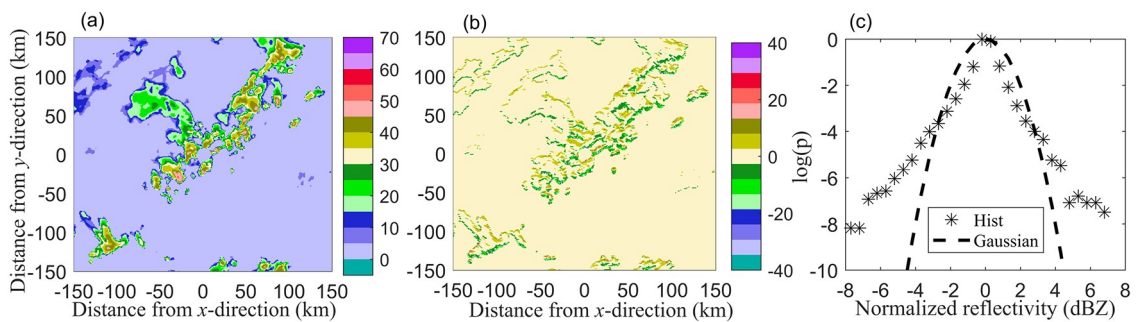


Fig. 2. (a) Radar reflectivity image of another precipitation case in Nanjing obtained at 0530:00 15 August 2010, (b) wavelet coefficients in the horizontal sub-band of the reflectivity image in (a), and (c) the corresponding log histogram (asterisks) of the wavelet coefficients normalized by the standard deviation.

tribution is $0.56N(0, 0.583) + 0.44N(0, 8.2958)$, where $N(0, 0.583)$ represents the Gaussian distribution function with mean 0 and variance 0.583. The coefficient of determination of the fitted line is 0.9872, and it can be seen from Fig. 1d that the GMM distribution can capture well the sharp peak and heavy tail of the precipitation image in the wavelet domain. By increasing the number of states, the arbitrary prob-

ability densities can be generated with a finite number of discontinuities. However, a GMM with more than two states may possess the problem of slow convergence speed and strong dependence on initial values, and it is easy to capture some local optimal values. Developing an optimized algorithm for a GMM with more states is a topic for further research. The two-state, zero-mean GMM is simple, robust,

and easy to use, which are attractive features for applications. In this study, a two-state GMM is employed.

In addition to the non-Gaussian and heavy-tail properties of the precipitation reflectivity, the data exhibit an evident interscale dependency because the precipitation fluctu-

ations are similar across scales and the wavelet transform does not completely decorrelate the precipitation images. Figure 4 shows the 2D joint and conditional histograms of the wavelet coefficients in the horizontal sub-band for the reflectivity image presented in Fig. 1b. The shape of the

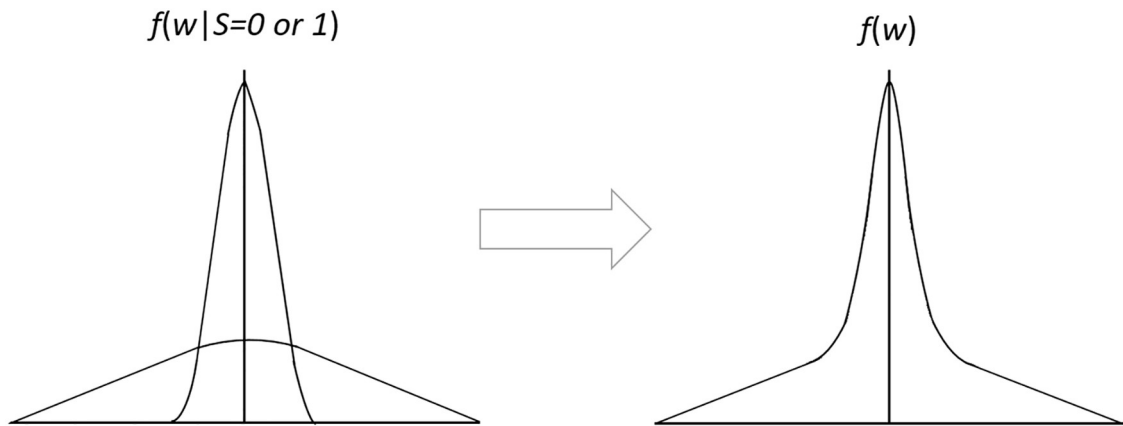


Fig. 3. Two-state, zero-mean GMM for a random variable used to generate a non-Gaussian probability distribution, where $s = 0$ or 1 denotes the state 0 or 1, $f(w|s=0$ or $1)$ is the Gaussian distribution under state 0 or 1, and $f(w)$ is the generated non-Gaussian distribution.

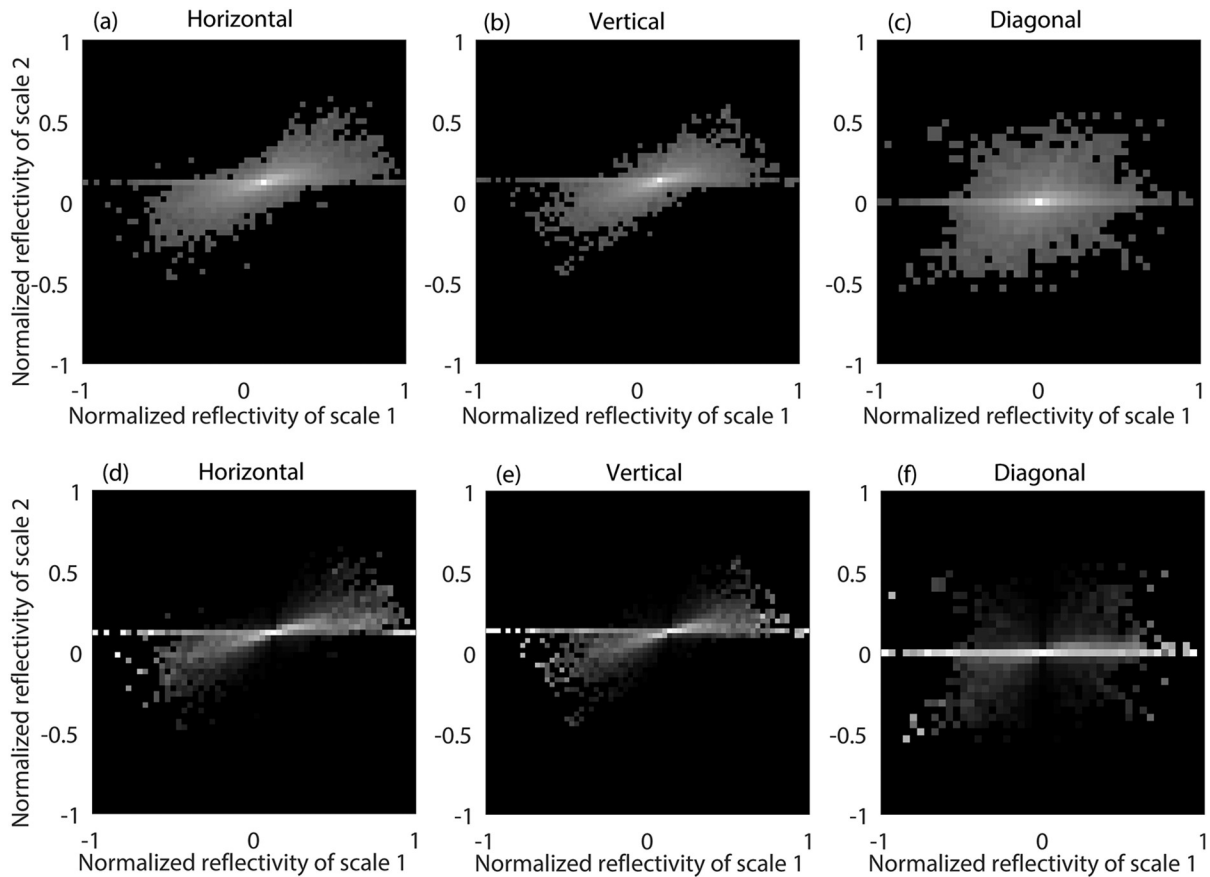


Fig. 4. Joint histogram of the (a) horizontal, (b) vertical and (c) diagonal wavelet coefficients of the precipitation reflectivity image in Fig. 1b, and (d–f) the corresponding conditional histograms. The shape of the joint histograms shows that the conditional probability of scale 2 given scale 1 is not uniform and that a high-order dependency exists. The bowtie shape of the conditional histograms demonstrates the interscale dependency, and the tilted shape indicates a nondiagonal covariance structure.

joint histograms in Figs. 4a–c indicates the conditional probability of scale 2 given that scale 1 is not uniform and that a high-order dependency exists. The shape of the conditional histograms in Figs. 4d–f indicates that the variance of scale 2 depends on the magnitudes of scale 1, and larger variance of scale 1 gives rise to scale 2 with larger variance. The tilted bowtie shapes of the horizontal and vertical sub-bands in Figs. 4d and e also represent the presence of off-diagonal nonzero elements on the covariance matrix of the scale-to-scale coefficients.

The marginal non-Gaussian distribution and scale-to-scale Markovian dependencies lead to practical HMT modeling for the precipitation reflectivity wavelet coefficients. The structure of the HMT model is shown in Fig. 5, where the solid points represent the wavelet coefficients and the hollow points denote the states of the coefficients. For example, w_1 is the wavelet coefficient at the root node and its state is indicated as s_1 . Every node can be related to the nodes at coarser and finer scales; in particular, the node $\rho(i)$ is the parent of node i .

The Markov tree structure shown in Fig. 5 has two implications. First, the state of the wavelet coefficients at any node i depends on the state of the coefficients at the parent node $\rho(i)$, and the dependence can be described by the

conditional probability:

$$P_{s_{\rho(i)}|s_i} (s_{\rho(i)} = m | s_i = n), \tag{2}$$

where $m \in \{0, 1\}$, $n \in \{0, 1\}$. Second, the wavelet coefficient representation in a quadtree structure of a multiscale Markov process can be expressed as a stochastic process evolving from the coarse scales to the fine scale according to

$$w(i) = A(i)w(\rho(i)) + B(i)e(i), \tag{3}$$

where $A(i)$ and $B(i)$ are the parameters that control the scale-to-scale variability of the process, $e(i) \sim N(0,1)$ is the Gaussian white noise, and the term $B(i)e(i)$ is called “process noise” with covariance $\Sigma_{B(i)}$.

2.2. Model parameter estimation

It is necessary to estimate three types of parameters in the HMT model—namely, the state decision, variance of Gaussian distribution, and multiscale process controlling parameters. First, the state probabilities of the GMM for the original (coarser scale) wavelet coefficients are estimated using the EM algorithm. Using the estimated state probabilities, the state of the parent coefficient is then determined by

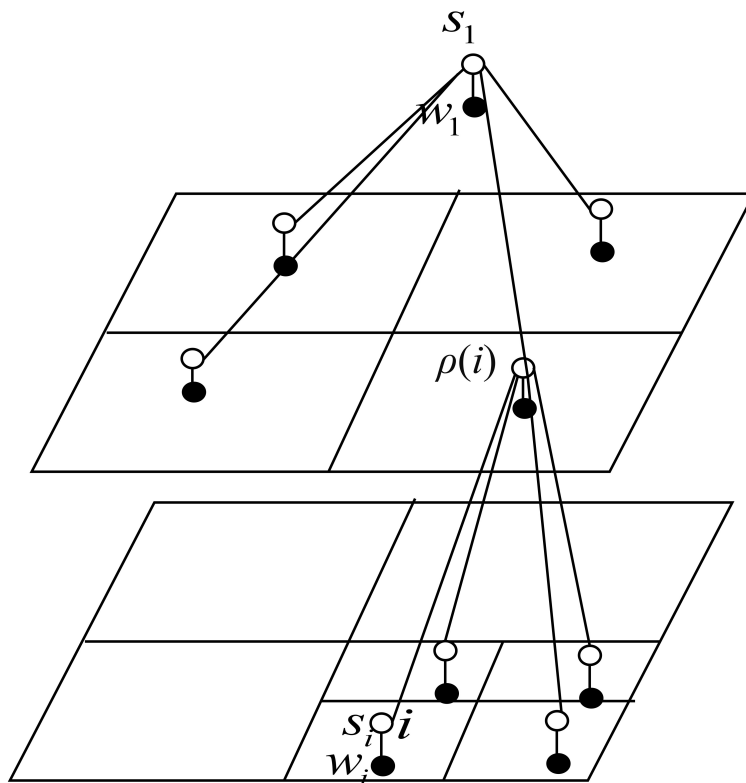


Fig. 5. Quadtree structure used to represent the HMT model, where the black node denotes the wavelet coefficient w_i and the white node denotes its state variable s_i ; in particular, w_1 and s_1 are coefficients and their state at the root node. In the representation, the GMM is used as the PDF for each wavelet coefficient, and every node is related to nodes at the coarser and finer scales (Markov dependency). For example, the state and coefficient at node i depend on its parent node $\rho(i)$.

calculating the expectation of the states within a local window:

$$E[s_{\rho(i)}] = \sum_m mP(s_{\rho(i)} = m), \quad (4)$$

$$P(s_{\rho(i)} = m) = \sum_n P(s_{\rho(i)} = m | s_i = n)P(s_i = n). \quad (5)$$

Considering the intrascale dependence of precipitation coefficients, a 5×5 window is employed. If $E[s_{\rho(i)}] \geq 0.5$, the parent coefficient belongs to state 1, and if not, state 0 is selected. The conditional state transition probability can be learned from a set of similar GR data, or the universal HMT parameters given by Romberg et al. (2001) can be used.

After the decision of the state, the variance of the Gaussian probability distribution is the next important parameter to be estimated. This parameter determines the precision of the shape of the GMM and the estimation of coefficient values. Due to the multifractal behavior and self-similarity of wavelet coefficients across scales (Deidda et al., 2006; Venugopal et al., 2006), the magnitude of variances decays exponentially as they are from coarse scales to finer scales. The relationship between the variances of consecutive scales can be described by

$$E[|w_{m,j}|^2] = 2^{\alpha_m} E[|w_{m,j-1}|^2], \quad (6)$$

where j denotes the scale, $m \in \{0, 1\}$, and α_m are the exponen-

tial decay constants.

Decomposing the precipitation reflectivity images at four levels ($j = 1-4$), the parameters α_m can be estimated by least-squares fitting. Figure 6 shows the evolution of the variance of the horizontal sub-band wavelet coefficients across scales, where Fig. 6a is obtained using the reflectivity data presented in Fig. 1b, and Fig. 6b is obtained using another precipitation case shown in Fig. 2a. The variance decay in the horizontal sub-band is measured with a log-scale plot of the variance versus scale for each state and total points, and the α_0 and α_1 parameters of the scaling law are 3.18 and 2.61 for Fig. 6a, and 3.07 and 2.56 for Fig. 6b.

The α_m vary in a finite range for different precipitation reflectivity images, enabling us to fix α_m to the average value obtained from a set of GR convective precipitation reflectivity images. Using 14 matched Nanjing GR datasets obtained between 2008 and 2010 and dominated by convective precipitation, the average and the interval of the α_m values are estimated, as summarized in Table 1 for all of the sub-band coefficients. This similarity reflects the statistical similarity of the precipitation images in the wavelet domain that is beneficial for the parameterization and is exploited as prior information.

After the Gaussian mixture probability distribution prior model is obtained, the finer-scale wavelet coefficients of radar reflectivity can be estimated in a multiscale framework using Eq. (3). It can be seen from Fig. 4 that the parameters $A(i)$ depend on the state covariances $\Sigma_{\rho(i)}$ and scale-

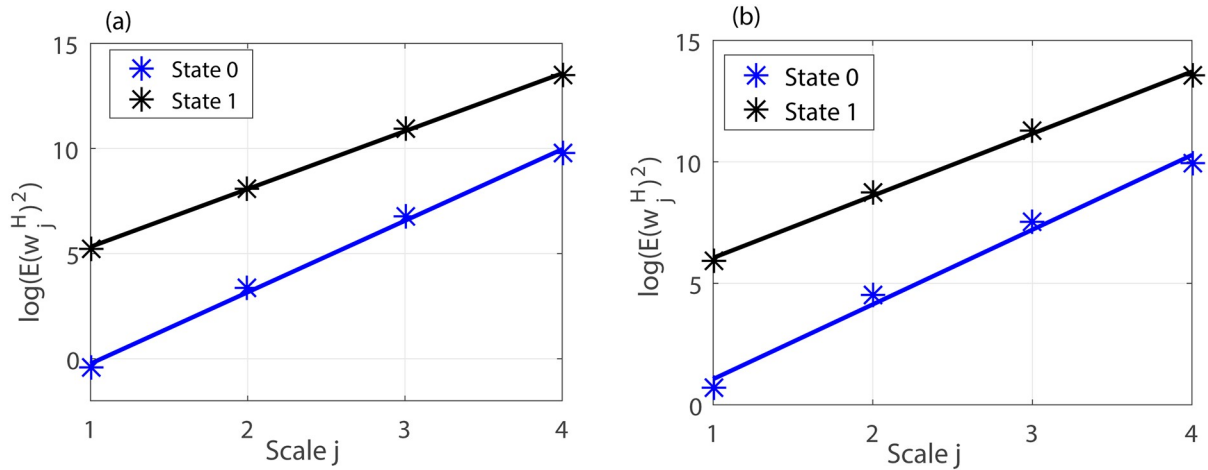


Fig. 6. Scaling law (in log form) of the horizontal sub-band wavelet coefficients across scales for the Nanjing GR precipitation reflectivity image obtained at 0456:41 UTC 27 May 2008 (a) and for the precipitation image obtained at 0536:00 UTC 15 August 2010 (b). Variance decay across scales (in log-log scale) for states 0 and 1 follow a linear law and can be used to characterize the evolution of the GMM distribution in the HMT model.

Table 1. Estimated decay parameters of variances for state 0 (α_0) and state 1 (α_1) at different orientations (H, horizontal; V, vertical; D, diagonal). The α_m ($m = 0$ or 1) vary in a finite range for different precipitation reflectivity images, and the average value of α_m obtained with 14 matched Nanjing GR data dominated by convective precipitation for 2008–10 is used.

	H	V	D
α_0	3.1151 (3.0477–3.2701)	3.0919 (3.0170–3.2545)	3.8094 (3.7735–3.9369)
α_1	2.5803 (2.4555–2.7211)	2.5022 (2.4738–2.5814)	2.7362 (2.6437–2.9221)

to-scale cross covariances $\Sigma_{(i,\rho(i))}$:

$$\mathbf{A}(i) = \frac{\Sigma_{(i,\rho(i))}}{\Sigma_{\rho(i)}}. \quad (7)$$

The $B(i)$ can be estimated from the difference between the fine-scale wavelet coefficient and the coefficient at the next coarser scale of the high-resolution GR reflectivity image,

$$B(i) = \sqrt{\text{Var}(\mathbf{w}(i)) - \text{Var}(\mathbf{w}(\rho(i)))}, \quad (8)$$

where $\text{Var}(\mathbf{w}(i))$ denotes the variance of the coefficients $\mathbf{w}(i)$. $B(i)$ is a function of scale, and the calculation should include the variance exponent decay across the scales.

3. Description of the interpolation algorithm

The estimation of the unknown wavelet coefficients in high-frequency sub-bands from coefficients in lower sub-bands is the key issue for interpolation in the wavelet domain. In contrast to traditional interpolation methods, such as bilinear interpolation, which inherently assume smoothness constraints, the wavelet transform decomposes the signal in different directions, which may preserve and reproduce the edges and local regularities (Demirel and Anbarjafari, 2011; Azam et al., 2014). For precipitation, and in particular for heavy convective precipitation, the sharp variation features, extreme values, and singularities are very important, because these features are relevant for hazard warning and forecasting. These features in the precipitation images typically correspond to the edges or boundaries in different directions between the wetted areas and the background, or between the high-intensity regions and the lower-intensity areas. The information about these features of precipitation can be obtained using a multiscale wavelet framework and statistical characteristics modeling.

The proposed interpolation algorithm will first capture and characterize the non-Gaussian structure (e.g., sharp variation and singularity) and interscale dependency (e.g., similarity across scales) of the radar reflectivity data, based on the multiscale wavelet analysis and HMT modeling. This characterization and HMT modeling are then used to estimate the value of the wavelet coefficients at the finest scale. The parameters of the HMT model will be estimated according to the description in section 2.2. Using the estimated parameters in the HMT model, the fine-scale wavelet coefficients for spaceborne radar can be generated according to Eq. (3) with Wiener filtering. The flow chart of the wavelet-based interpolation of spaceborne radar reflectivity data based on the HMT model is shown in Fig. 7.

The algorithm can be summarized as follows:

A set of matched GR reflectivity images dominated by convective precipitation is decomposed with a shift-invariant undecimated orthogonal wavelet transform and Haar wavelet base, from which the multiscale wavelet coefficients in horizontal, vertical, and diagonal sub-bands are

obtained.

Due to the local coherence of the wavelet coefficients, the wavelet coefficients in each sub-band are divided into overlapping 5×5 local windows.

The parameters of the state probabilities $P_{s_i}(m)$ are estimated from the original spaceborne radar image using the EM algorithm, and the conditional state transition probabilities $P(s_{\rho(i)} = m | s_i = n)$ in the HMT model of wavelet coefficients are estimated from the GR reflectivity images, where $m \in \{0, 1\}$.

Based on the interscale dependence of wavelet coefficients across scales, the self-similarity index of the α_m of variance evolution, the transition matrix $\mathbf{A}(i)$, and process noise $B(i)$, are calculated from the GR precipitation reflectivity images.

Due to the undecimated processing of the wavelet transform used to avoid the aliasing effect, the spaceborne PR reflectivity images are interpolated using a bilinear algorithm to ensure that the pixel size of the interpolated spaceborne PR image is the same as that of the expected high-resolution image.

The interpolated spaceborne radar reflectivity images are decomposed, and the wavelet coefficients in each sub-band are divided with an overlapping 5×5 window. Then, the elements of a neighborhood of the wavelet coefficients are stacked according to a fixed order into a vector form \mathbf{y} .

Using the prior HMT model parameters, the state m is determined using Eqs. (4) and (5), and the wavelet coefficient vector \mathbf{x} at finer scale is estimated locally according to Eq. (9) using Wiener filtering for every neighborhood location that slides over the entire sub-band domain. In Eq. (9), Σ_m denotes the covariance matrix of the wavelet coefficients belonging to the state m :

$$\mathbf{x} = \Sigma_m \mathbf{A}^T (\mathbf{A} \Sigma_m \mathbf{A}^T + \Sigma_B)^{-1} \mathbf{y}. \quad (9)$$

For all overlapping areas, the estimated coefficients are averaged to obtain the final wavelet coefficients at high-pass sub-bands. The high-resolution spaceborne PR image is obtained with the estimated wavelet coefficients using an inverse wavelet transform.

It is worth noting that the background effect of rainfall fields is significant. At each level of the wavelet decomposition, due to the convolution of the field with the wavelet scaling function, a set of zero values next to edges of the wetted areas becomes nonzero and subsequently the areas of nonzero pixels progressively grow from fine to coarse scales. For resolving this issue, the background pixels (zeros) of the coarse resolution spaceborne radar image remain zero in the finer scale image.

4. Results from the case studies

There are inherent differences in the reflectivity of the two instruments (TRMM PR and GR) owing to their different frequencies, sampling characteristics, sample volumes, and so on (Wang and Wolff, 2009; Warren et al., 2018). For

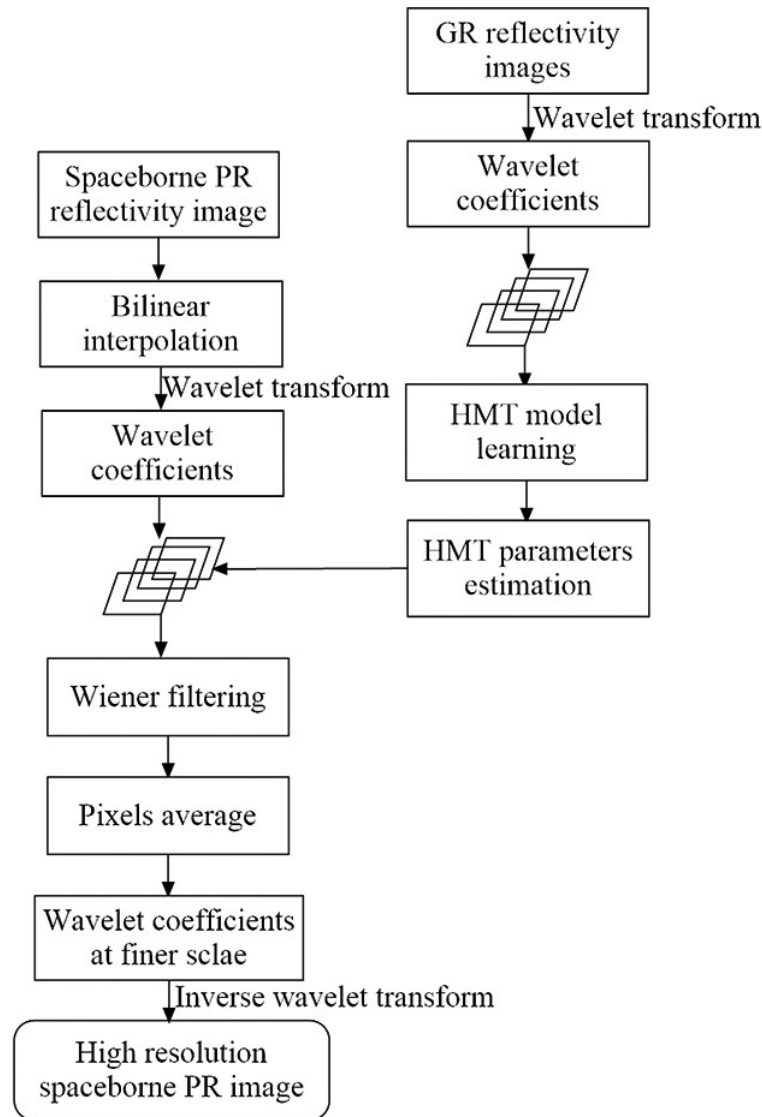


Fig. 7. Flow chart of the wavelet-based interpolation for spaceborne radar reflectivity with the HMT model as prior information.

merely considering the interpolation method itself, a case from the Nanjing GR on 25 July 2011 that was not included in the GR training dataset was firstly selected to demonstrate the effectiveness of the proposed algorithm. The original GR data at $1 \text{ km} \times 1 \text{ km}$ (Fig. 8a) were downgraded to $4 \text{ km} \times 4 \text{ km}$ low-resolution observations via a simple box-averaging of size 4×4 , followed by downsampling with a factor of 4. The resulting low-resolution field is shown in Fig. 8b, and it can be considered to be the field that would be available to us from a satellite sensor. By using the prior HMT modeling in the wavelet domain, a high-resolution interpolation reflectivity field (from $4 \text{ km} \times 4 \text{ km}$ to $1 \text{ km} \times 1 \text{ km}$) is generated in Fig. 8d. For comparison, the result with bilinear interpolation is shown in Fig. 8c. The results in Fig. 8 show that, due to the explicit consideration of the heavy-tail nature and interscale dependent structure of the wavelet coefficients of the precipitation reflectivity data, the proposed method can reproduce the spatial correlation of

the precipitation images while accounting for the non-Gaussian marginal statistics and heavy-tail features. This result is promising in that it demonstrates the method can recover the high-frequency features and estimate the small-scale structures of the precipitation image of interest for a relatively coarse-scale observation.

Table 2 presents a statistical comparison of the images in Fig. 8 in terms of several quantitative parameters—namely, the mean error (MEAN), the root-mean-square error (RMSE), the peak signal-to-noise ratio (PSNR), and the Kullback–Leibler divergence (KLD). These parameters are calculated as follows (Gonzalez and Woods, 2007):

$$\text{MEAN} = \|f - f_0\|_1 / N, \quad (10)$$

$$\text{RMSE} = \|f - f_0\|_2 / \sqrt{N}, \quad (11)$$

$$\text{PSNR} = 20 \lg[\max(f) / \text{RMSE}], \quad (12)$$

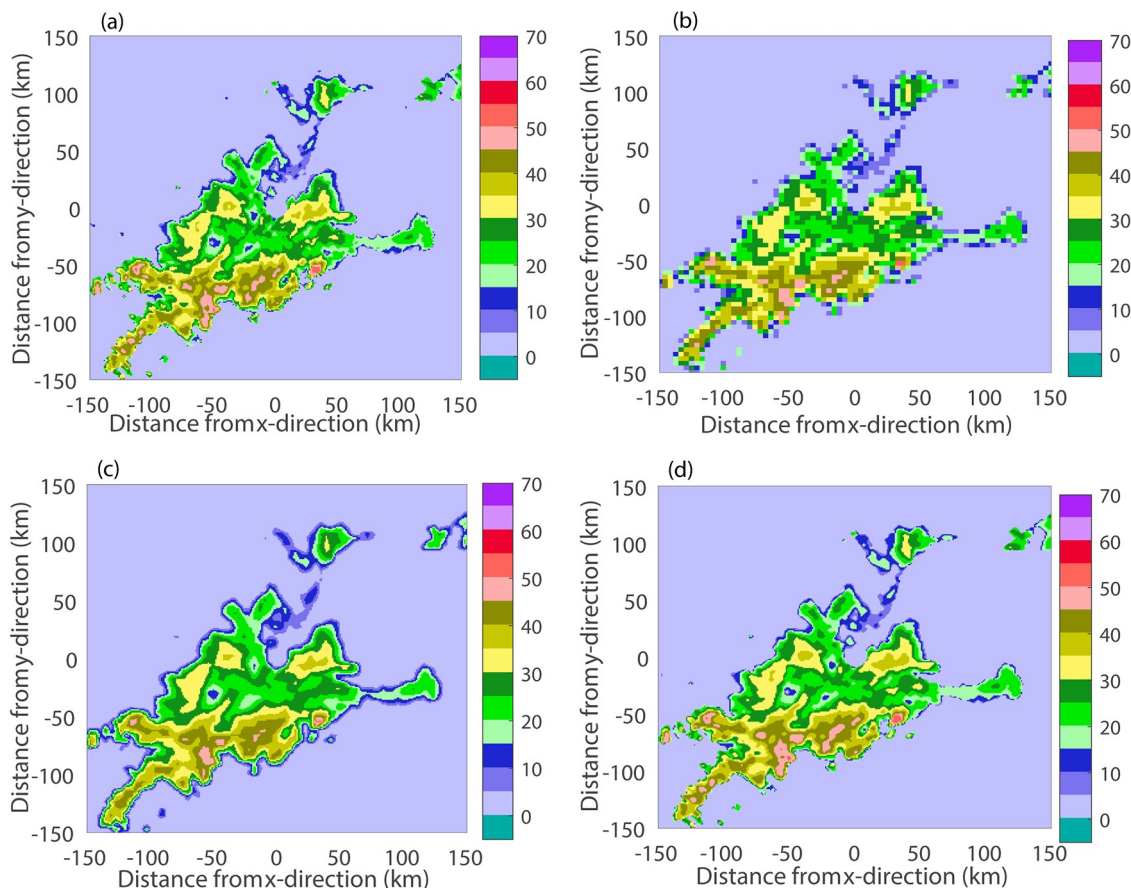


Fig. 8. Comparisons of radar reflectivity images from the Nanjing GR at 2302:00 UTC 25 July 2011: (a) the original high-resolution GR reflectivity image at resolution $1 \text{ km} \times 1 \text{ km}$; (b) the coarse-scale image at resolution $4 \text{ km} \times 4 \text{ km}$ generated by smoothing and downsampling; (c) the GR image with bilinear interpolation; and (d) the high-resolution wavelet-based interpolation result with HMT prior modeling.

Table 2. Error statistics obtained by comparing the original high-resolution GR precipitation reflectivity image obtained on 25 July 2011 (the reference) with the bilinearly interpolated GR image from the smoothed low-resolution GR (GR with bilinear for short) and that obtained by HMT prior modeling in the wavelet domain (GR with HMT for short).

	MEAN	RMSE	PSNR	KLD
GR with bilinear	1.1242	3.6512	25.4204	0.1028
GR with HMT	0.2834	1.7751	28.8759	0.038

$$\text{KLD} = \sum_i p_{f_0}(i) \ln \left[\frac{p_{f_0}(i)}{p_f(i)} \right], \quad (13)$$

where $\|f\|_1$ denotes the l_1 -norm, $\|f\|_2$ denotes the l_2 -norm, and $p_{f_0}(i)$ and $p_f(i)$ are the discrete probabilities of the true data (f_0) and the estimated data (f). The original high-resolution GR image is used as the reference f_0 . In Table 2, the PSNR (in units of dB) represents a measure that not only contains the RMSE but also encodes the recovered range, which reflects the closeness of the estimated values to the reference data, so that a high PSNR value indicates a high quality reconstructed image. The KLD is the relative entropy, which represents the relative degree of closeness between

two probability distributions in terms of their entropy, where smaller values signify a stronger degree of similarity. It can be seen from Table 2 that the proposed method produces a high-resolution precipitation field that is closer to the original high-resolution GR field and can better reproduce the extreme intensities and local gradients with larger PSNR and smaller KLD. Compared to bilinear interpolation, the PSNR of the image with HMT modeling in the wavelet domain shows improvement on an order of 3 to 4 dB, and the KLD index has an improvement of about 60%–70%.

For demonstrating the stability and robustness of the algorithm, more different convective precipitation cases from the Nanjing GR during the summer (from May to September) of 2011 were processed in similar way, as shown by the images in Fig. 8, and the statistical comparison results are presented in Table 3. The cases in Table 3 span a wide range of heavy precipitation with different spatial structures and geometrical shapes, ranging from clustered convective cells to frontal convective lines. The first column lists the dates of the precipitation cases. From Table 3, it can be seen that the proposed wavelet-based interpolation method generally outperforms the result obtained

Table 3. Error statistics obtained by comparing the original high-resolution GR precipitation reflectivity images (Cases) obtained from the Nanjing GR during the summer of 2011 with the bilinearly interpolated GR images from the smoothed low-resolution GR (GR with bilinear for short) and those obtained by HMT prior modeling in the wavelet domain (GR with HMT for short).

Case	Methods	MEAN	RMSE	PSNR	KLD
20110617	GR with bilinear	1.2530	4.5483	19.9765	0.0981
	GR with HMT	0.3849	4.1850	22.5394	0.0484
20110623	GR with bilinear	0.8260	3.3452	23.4702	0.1087
	GR with HMT	0.3276	3.6212	27.3611	0.0640
20110711	GR with bilinear	0.9756	3.1947	24.8578	0.0906
	GR with HMT	0.2925	1.8755	27.0366	0.0583
20110718	GR with bilinear	1.4812	4.1528	20.4720	0.1138
	GR with HMT	0.4198	3.8849	22.6933	0.0752
20110725	GR with bilinear	1.1242	3.6512	25.4204	0.1028
	GR with HMT	0.2834	1.7751	28.8759	0.0380
20110811	GR with bilinear	1.5021	4.4328	21.5048	0.1187
	GR with HMT	0.5277	3.6794	24.0597	0.0445
20110817	GR with bilinear	0.9565	3.8124	23.9025	0.0899
	GR with HMT	0.3014	2.9140	26.2355	0.0341
Average	GR with bilinear	1.1598	3.8768	22.8006	0.1032
	GR with HMT	0.3624	3.1336	25.5430	0.0518

via bilinear interpolation. The MEAN decreases by about 60% and the RMSE decreases by about 20% on average, by comparing the results of the proposed method with the results of bilinear interpolation. In terms of the PSNR, the HMT method shows improvement on an order of 2 to 4 dB, and the KLD index is also improved (50%–70%). The wavelet-based HMT method can better reproduce the small-scale structures and variability features compared to the conventional spatial interpolation method, due to the inclusion of prior statistical information, such as the non-Gaussian marginal distribution of convective precipitation. Note that the algorithm can be used for images at other heights or from other radar stations, as long as the model parameters are correctly estimated. The performance for images at 1 km height is similar to those at 3 km height in Table 3 (not shown here). However, it should also be noted that the algorithm's ability to properly reproduce the high-resolution structures and detailed features may be limited if the original low-resolution image is too smooth with little high-frequency information.

To further demonstrate the application of the HMT modeling and the proposed wavelet-based interpolation algorithm on spaceborne radar reflectivity, two cases of convective precipitation from TRMM PR were selected to evaluate the performance quantitatively. Figure 9 shows images for a convective storm that occurred in Nanjing on 27 May 2008. The storm was caused by the joint effects of the eastward movement of a low trough in the upper air, low-level shear, and southward cold air. The storm image obtained by TRMM PR with a resolution of $4 \text{ km} \times 4 \text{ km}$ is shown in Fig. 9a, and the coincidental image from the Nanjing GR is shown in Fig. 9b, with a resolution of $1 \text{ km} \times 1 \text{ km}$. For comparison, the TRMM PR image is interpolated using the bilinear method, presented in Fig. 9c. Figure 9d shows the result

obtained by the wavelet-based interpolation of the TRMM PR data from the resolution of $4 \text{ km} \times 4 \text{ km}$ to the resolution of $1 \text{ km} \times 1 \text{ km}$ using the proposed method with HMT prior modeling. It can be seen from Fig. 9c that the bilinear interpolation smooths the image without adequate detailed features of the storm and extreme intensity values, due to its low-pass filtering effect. The result presented in Fig. 9d demonstrates that the proposed method can estimate the small-scale detailed structures of the precipitation and incorporates more information from the TRMM PR data. The 1D reflectivity data shown in Fig. 9e demonstrate that the curve of the original TRMM PR image is relatively smooth, and the reconstructed curve shows more fluctuations, with the result much closer to the high-resolution GR data. This confirms that the reconstructed image can reproduce more detailed information, such as sharp gradients and extreme values, compared to the original low-resolution TRMM PR image.

Table 4 presents a quantitative comparison of the interpolation results for TRMM PR in Fig. 9. Although the reference high-resolution rainfall field is of course not available in practical cases, and differences exist in the reflectivity from the TRMM PR and the GR, it is instructive to make a quantitative assessment by comparing the TRMM PR interpolation results with the spatiotemporally matched GR data [the reference (f_0)]. The reflectivity of the original low-resolution TRMM PR (Original PR), bilinearly interpolated TRMM PR (Bilinear), and wavelet-based interpolated TRMM PR with HMT modeling (HMT) methods are compared to the reference GR data. For comparison, the data pairs are selected in the area where both the TRMM PR and GR data are available. Note that to compute the quantitative parameters of the original low-resolution observations of TRMM PR, the size of those fields was extended to the

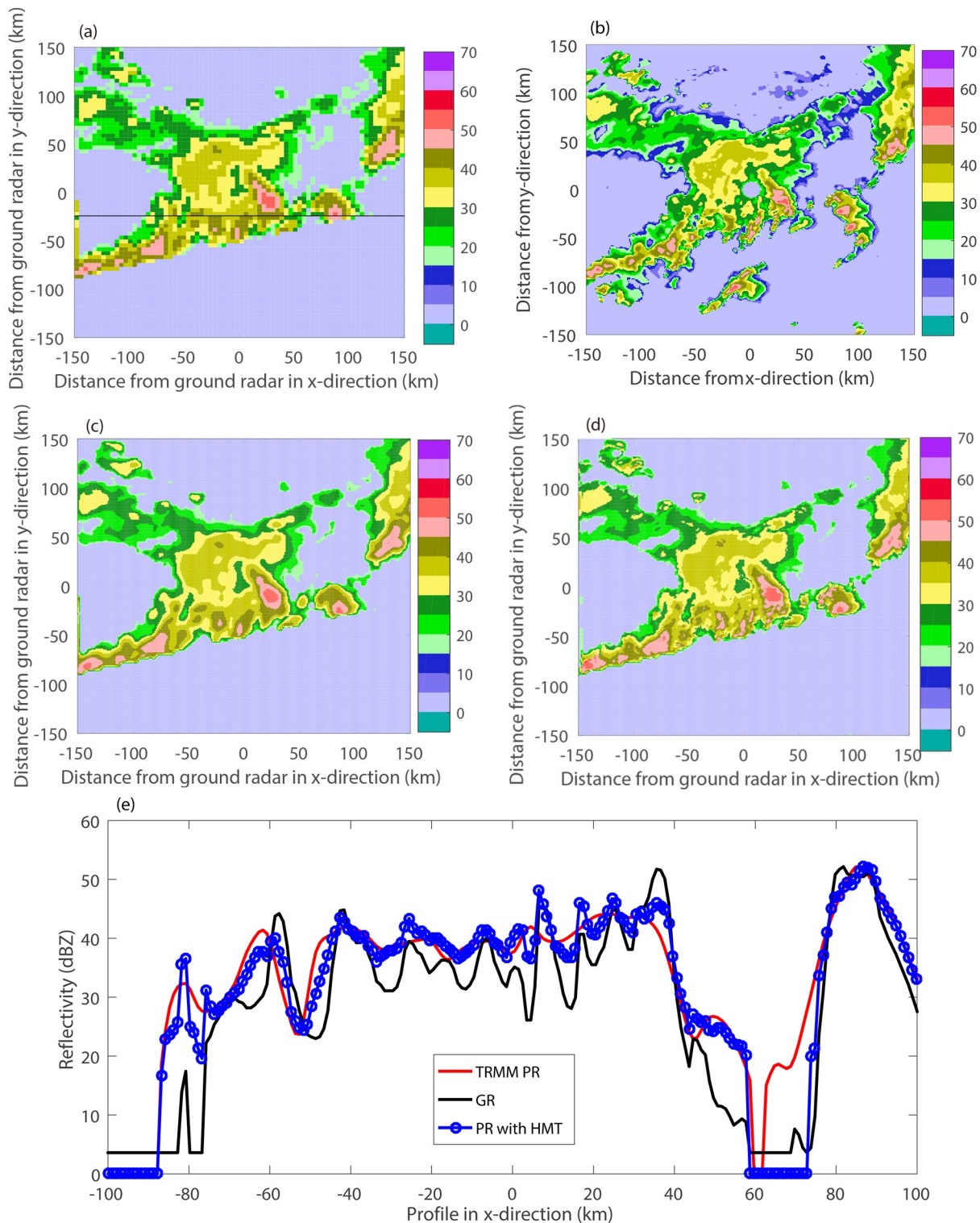


Fig. 9. Comparisons of the reflectivity images for the case of convective precipitation in Nanjing at 0459:00 UTC 27 May 2008: (a) TRMM PR; (b) GR; (c) TRMM PR image with bilinear interpolation; (d) wavelet-based interpolated TRMM PR image with HMT prior modeling; (e) reflectivity profiles along the line in (a), where the red, black and blue lines denote the TRMM PR data, the GR data, and the wavelet-based interpolated data, respectively. For quantitative comparison, please refer to Table 3.

size of the true field using nearest neighborhood interpolation. The results in Fig. 9 and Table 3 show that the proposed method produces high-resolution spaceborne radar pre-

cipitation fields that are closer to the structure of the high-resolution GR field, and that the HMT method considerably outperforms the simple spatial interpolation method, such as

Table 4. Error statistics obtained by comparing the matched high-resolution GR precipitation reflectivity image obtained on 27 May 2008 (the reference) with the original TRMM PR image (Original PR for short), the interpolated PR image obtained using the bilinear algorithm (Bilinear for short), and that obtained by HMT prior modeling in the wavelet domain (HMT for short).

	MEAN	RMSE	PSNR	KLD
Original PR	2.8505	5.9736	19.0184	0.1158
Bilinear	2.7900	5.4182	19.7585	0.0951
HMT	1.7818	4.2253	21.9953	0.0781

the result obtained by bilinear interpolation. Due to the difference from the two instruments (TRMM PR and GR), from Table 4 it can be seen that the degree of improvement is lower than the result in Table 2. The PSNR of the spaceborne radar image reconstructed with HMT modeling shows an improvement on the order of approximately 2–3 dB, and the KLD is improved by about 30%.

Figure 10 and Table 5 show the images and the quantitative statistical results for the case on 17 August 2011, when the precipitation was not included in the dataset for HMT

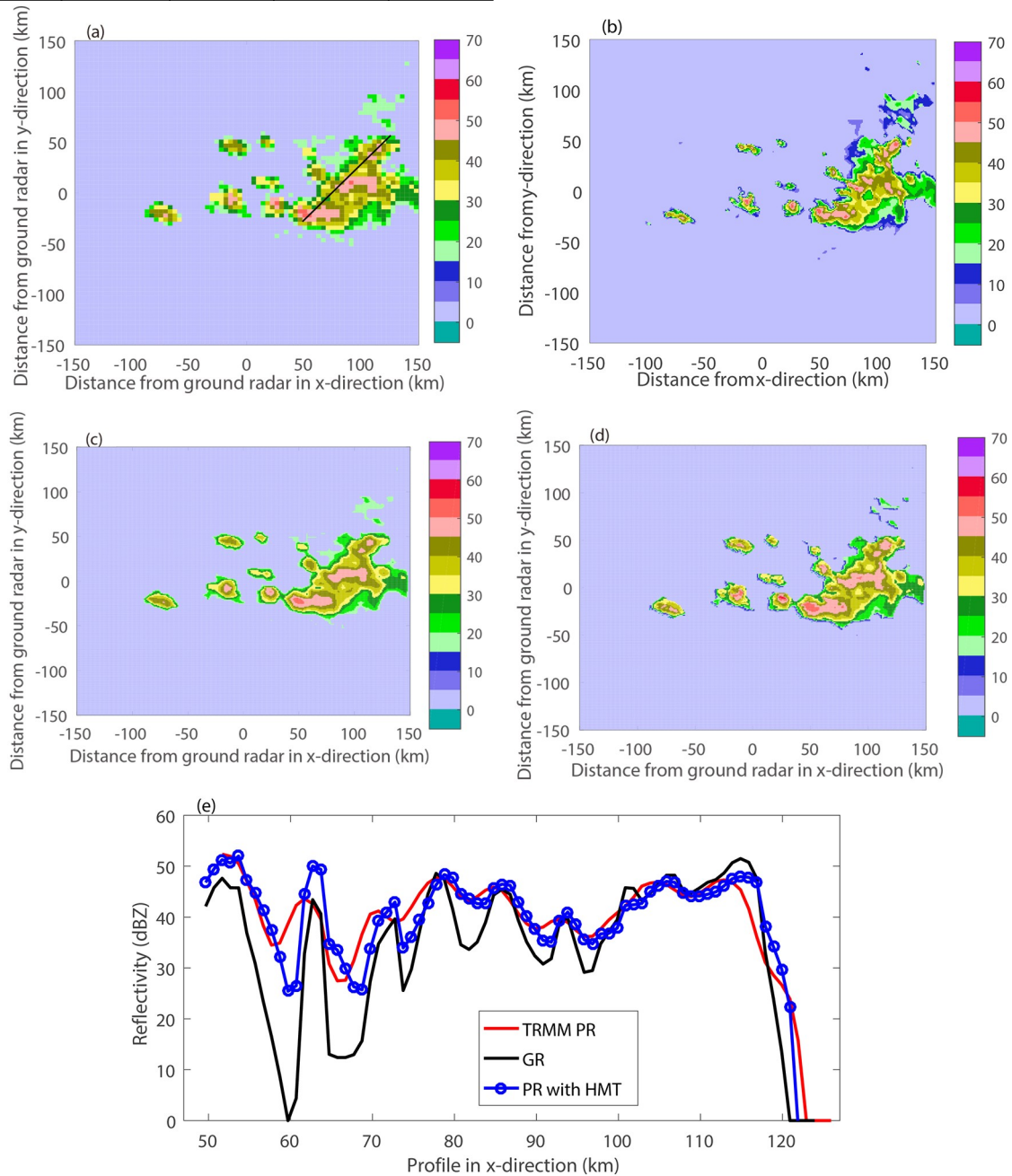


Fig. 10. Comparisons of the reflectivity images for the case of convective precipitation in Nanjing at 0815:00 UTC 17 August 2011: (a) TRMM PR; (b) GR; (c) TRMM PR image with bilinear interpolation; (d) wavelet-based interpolated TRMM PR image with HMT prior modeling; (e) reflectivity profiles along the line in (a), where the red, black and blue lines denote the TRMM PR data, the GR data, and the wavelet-based interpolated data, respectively. For quantitative comparison, please refer to Table 4.

Table 5. Error statistics obtained by comparing the matched high-resolution GR precipitation reflectivity image obtained on 17 August 2011 (the reference) with the original TRMM PR image (Original PR for short), the interpolated PR image obtained using the bilinear algorithm (Bilinear for short), and that obtained by HMT prior modeling in the wavelet domain (HMT for short).

	MEAN	RMSE	PSNR	KLD
Original PR	3.2823	7.5839	17.0690	0.0848
Bilinear	2.8304	7.6223	16.8632	0.0754
HMT	2.4350	6.3491	18.0984	0.0523

modeling. From the interpolation results it can be seen that, with prior knowledge containing important statistical characteristics such as the non-Gaussian structure of convective precipitation data, the high-frequency features and small-scale geometrical structures can be recovered with the proposed method. An examination of the horizontal profiles presented in Fig. 10e shows that the wavelet-based interpolated reflectivity image exhibits obvious fluctuations and gradients compared to the low-resolution TRMM PR data, and its structure is more similar to the high-resolution GR image.

To better illustrate the improvement of the statistical properties of the thicker-than-Gaussian tails of precipitation gradients, in Fig. 11 we compare the probability distribution of the derivatives in the horizontal direction in terms of a Q–Q plot, where the x -coordinates are the standard normal quantiles and the y -coordinates are the quantiles of standardized reflectivity derivatives. All of the PDFs presented in Fig. 11 differ strongly from a Gaussian distribution (black dashed straight line), and the PDF of the high-resolution GR data (black dotted line) shows a more obvious heavy tail compared to the PDF of the low-resolution TRMM PR data (line with red crosses), while the PDF of the wavelet-based interpolated data with HMT modeling (blue diamonds) is in between. It can be seen that the wavelet-based interpolation method with HMT modeling can reproduce the heavy tail of

the PDF of precipitation gradients, which are thicker than those of the TRMM PR PDF. It is clear that the high-resolution image is much finer, and the wavelet-based interpolated image is able to enhance the tails of the low-resolution precipitation reflectivity and reproduce the high gradients in the high-resolution precipitation field.

5. Conclusions

Based on the statistical characteristics of convective precipitation reflectivity data, an HMT model in the wavelet domain is introduced as prior information. The HMT model can effectively capture the multiscale structure of the wavelet coefficients of precipitation, including the heavy-tailed non-Gaussian distribution, interscale dependency, and the nonlinear scaling law (multifractal behavior). The problem of high-resolution interpolation of spaceborne radar precipitation data in the wavelet domain is equivalent to the problem of estimating the coefficients at finer scales. The prior HMT model used to interpolate the spaceborne radar precipitation data in the wavelet domain can improve the resolution of precipitation, while effectively reproducing and preserving the desired precipitation properties such as extreme intensities, steep gradients and singularities. Because of the similar statistical properties and common mathematical signatures in the radar reflectivity data, the parameters of the prior model can be estimated from a set of available coincidental spaceborne and GR precipitation observations dominated by convective precipitation. Most parameters of the prior HMT model, including the conditional state transition probability, variance decaying parameters, and scale-to-scale process controlling parameters, are estimated from high-resolution GR data. This is flexible and will be important for addressing optimal estimation problems such as spaceborne radar data interpolation, physical parameter retrieval, and multisensor precipitation data fusion.

In this study, a two-state Gaussian mixture distribution was used in the HMT modeling, which is conditionally Gaus-

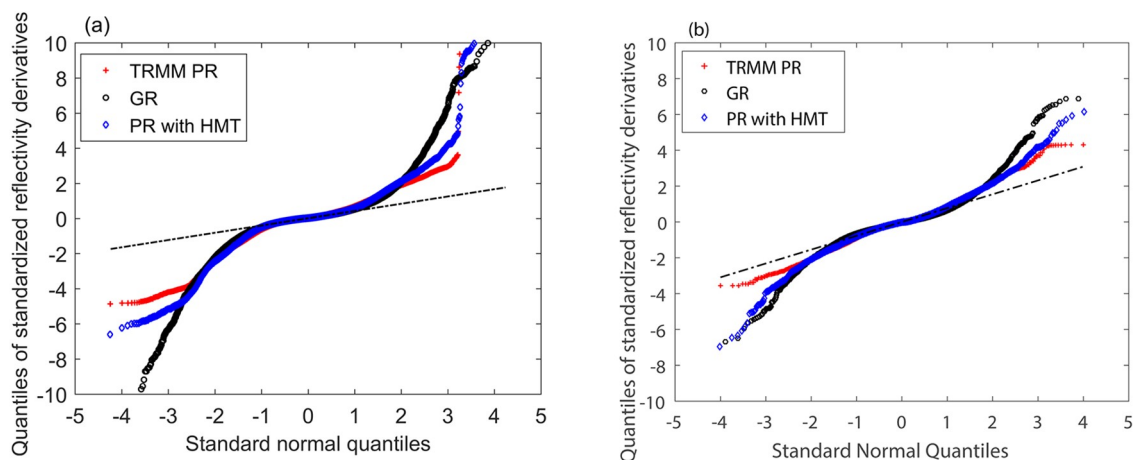


Fig. 11. Quantiles of the standardized horizontal derivatives versus standard normal quantiles, where red crosses, black circles and blue diamonds denote the original TRMM PR data, the matched high-resolution GR data, and the wavelet-based interpolated TRMM PR data with HMT modeling, respectively: (a) precipitation case on 27 May 2008; (b) precipitation case on 17 August 2011. The dashed straight line represents Gaussian distribution quantiles.

sian given another state. The property of the conditional Gaussian distribution is convenient and advantageous for linear optimal estimation problems. However, a two-state Gaussian mixture distribution is not sufficiently flexible. A wavelet-based HMT model with more than two states, and its application to radar reflectivity data, will be studied in further research.

Acknowledgements. This study was funded by the National Natural Science Foundation of China (Grant No. 41975027), the Natural Science Foundation of Jiangsu Province (Grant No. BK20171457), and the National Key R&D Program on Monitoring, Early Warning and Prevention of Major Natural Disasters (Grant No. 2017YFC1501401).

REFERENCES

- Azam, S., F. T. Zohra, and M. M. Islam, 2014: A state-of-the-art review on wavelet based image resolution enhancement techniques: Performance evaluation criteria and issues. *IJ. Image, Graphics and Signal Processing*, **6**, 35–46, <https://doi.org/10.5815/ijgisp.2014.09.05>.
- Badas, M. G., R. Deidda, and E. Piga, 2006: Modulation of homogeneous space-time rainfall cascades to account for orographic influences. *Natural Hazards and Earth System Sciences*, **6**, 427–437, <https://doi.org/10.5194/nhess-6-427-2006>.
- Chavez-Roman, H., and Y. Ponomaryov, 2014: Super resolution image generation using wavelet domain interpolation with edge extraction via a sparse representation. *IEEE Geoscience and Remote Sensing Letters*, **11**, 1777–1781, <https://doi.org/10.1109/LGRS.2014.2308905>.
- Crouse, M. S., R. D. Nowak, and R. G. Baraniuk, 1998: Wavelet-based statistical signal processing using hidden Markov models. *IEEE Transactions on Signal Processing*, **46**, 886–902, <https://doi.org/10.1109/78.668544>.
- Deidda, R., 2000: Rainfall downscaling in a space-time multifractal framework. *Water Resour. Res.*, **36**, 1779–1794, <https://doi.org/10.1029/2000WR900038>.
- Deidda, R., M. G. Badas, and E. Piga, 2006: Space-time multifractality of remotely sensed rainfall fields. *J. Hydrol.*, **322**, 2–13, <https://doi.org/10.1016/j.jhydrol.2005.02.036>.
- Demirel, H., and G. Anbarjafari, 2011: Image resolution enhancement by using discrete and stationary wavelet decomposition. *IEEE Transactions on Image Processing*, **20**, 1458–1460, <https://doi.org/10.1109/TIP.2010.2087767>.
- Ebtehaj, M., and E. Foufoula-Georgiou, 2011: Statistics of precipitation reflectivity images and cascade of Gaussian-scale mixtures in the wavelet domain: A formalism for reproducing extremes and coherent multiscale structures. *J. Geophys. Res.*, **116**, D14110, <https://doi.org/10.1029/2010JD015177>.
- Ebtehaj, A. M., and E. Foufoula-Georgiou, 2013: On variational downscaling, fusion, and assimilation of hydrometeorological states: A unified framework via regularization. *Water Resour. Res.*, **49**, 5944–5963, <https://doi.org/10.1002/wrcr.20424>.
- Ebtehaj, A. M., E. Foufoula-Georgiou, and G. Lerman, 2012: Sparse regularization for precipitation downscaling. *J. Geophys. Res.*, **117**, 1–12, <https://doi.org/10.1029/2011JD017057>.
- Figueiredo, M. A. T., and R. D. Nowak, 2003: An EM algorithm for wavelet-based image restoration. *IEEE Transactions on Image Processing*, **12**, 906–916, <https://doi.org/10.1109/TIP.2003.814255>.
- Foufoula-Georgiou, E., A. M. Ebtehaj, S. Q. Zhang, and A. Y. Hou, 2014: Downscaling satellite precipitation with emphasis on extremes: A variational 11-norm regularization in the derivative domain. *Surveys in Geophysics*, **35**, 765–783, <https://doi.org/10.1007/s10712-013-9264-9>.
- Gonzalez, R. C., and R. E. Woods, 2007: *Digital Image Processing*, 3rd ed., Upper Saddle River, 1184 pp.
- Gupta, R., V. Venugopal, and E. Foufoula-Georgiou, 2006: A methodology for merging multisensor precipitation estimates based on expectation–maximization and scale-recursive estimation. *J. Geophys. Res.*, **111**, D02102, <https://doi.org/10.1029/2004JD005568>.
- Harris, D., E. Foufoula-Georgiou, K. K. Droegemeier, and J. J. Levit, 2001: Multiscale statistical properties of a high-resolution precipitation forecast. *J. Hydrometeorol.*, **2**, 406–418, [https://doi.org/10.1175/1525-7541\(2001\)002<0406:MSPOAH>2.0.CO;2](https://doi.org/10.1175/1525-7541(2001)002<0406:MSPOAH>2.0.CO;2).
- Hou, A. Y., and Coauthors, 2014: The global precipitation measurement mission. *Bull. Amer. Meteor. Soc.*, **95**, 701–722, <https://doi.org/10.1175/BAMS-D-13-00164.1>.
- Jiao, P. C., Z. H. Wang, Z. G. Chu, J. Han, S. Zhang, and Y. Q. Zhu, 2016: An interpolation method for weather radar data based on Fourier spectrum analysis. *Plateau Meteorology*, **35**, 1683–1693, <https://doi.org/10.7522/j.issn.1000-0534.2015.00108>. (in Chinese with English abstract)
- Kou, L. L., Z. H. Wang, and F. Xu, 2018: Three-dimensional fusion of spaceborne and ground radar reflectivity data using a neural network-based approach. *Adv. Atmos. Sci.*, **35**, 346–359, <https://doi.org/10.1007/s00376-017-6334-9>.
- Kou, L. L., Z. H. Wang, F. F. Shen, and Z. G. Chu, 2019: High resolution interpolation for weather radar data based on Gaussian-scale mixtures model in wavelet domain. *Acta Meteorologica Sinica*, **77**, 142–153, <https://doi.org/10.11676/qxxb2019.001>. (in Chinese with English abstract)
- Kozu, T., and Coauthors, 2001: Development of precipitation radar onboard the Tropical Rainfall Measuring Mission (TRMM) satellite. *IEEE Trans. Geosci. Remote Sens.*, **39**, 102–116, <https://doi.org/10.1109/36.898669>.
- Li, F., X. P. Jia, D. Fraser, and A. Lambert, 2010: Super resolution for remote sensing images based on a universal hidden Markov tree model. *IEEE Trans. Geosci. Remote Sens.*, **48**, 1270–1278, <https://doi.org/10.1109/TGRS.2009.2031636>.
- Liao, L., and R. Meneghini, 2009: Validation of TRMM precipitation radar through comparison of its multiyear measurements with ground-based radar. *J. Appl. Meteorol. Clim.*, **48**, 804–817, <https://doi.org/10.1175/2008JAMC1974.1>.
- Nason, G. P., and B. W. Silverman, 1995: The stationary wavelet transform and some statistical applications. *Wavelets and Statistics*, A. Antoniadis and G. Oppenheim, Eds., Springer, 918–936, https://doi.org/10.1007/978-1-4612-2544-7_17.
- Perica, S., and E. Foufoula-Georgiou, 1996: Model for multiscale disaggregation of spatial rainfall based on coupling meteorological and scaling descriptions. *J. Geophys. Res.*, **101**, 26 347–26 361, <https://doi.org/10.1029/96JD01870>.
- Prakash, S., A. K. Mitra, D. S. Pai, and A. AghaKouchak, 2016: From TRMM to GPM: How well can heavy rainfall be detected from space? *Advances in Water Resources*, **88**, 1–7, <https://doi.org/10.1016/j.advwatres.2015.11.008>.

- Romberg, J. K., H. Choi, and R. G. Baraniuk, 2001: Bayesian tree-structured image modeling using wavelet-domain hidden Markov models. *IEEE Transactions on Image Processing*, **10**, 1056–1068, <https://doi.org/10.1109/83.931100>.
- Ruzanski, E., and V. Chandrasekar, 2015: Weather radar data interpolation using a Kernel-based Lagrangian Nowcasting technique. *IEEE Trans. Geosci. Remote Sens.*, **53**, 3073–3083, <https://doi.org/10.1109/TGRS.2014.2368076>.
- Sapozhnikov, V. B., and E. Foufoula-Georgiou, 2007: An exponential Langevin-type model for rainfall exhibiting spatial and temporal scaling. *Nonlinear Dynamics in Geosciences*, A. A. Tsonis and J. B. Elsner, Eds., Springer, 87–100, https://doi.org/10.1007/978-0-387-34918-3_6.
- Skofronick-Jackson, G., and Coauthors, 2017: The global precipitation measurement (GPM) mission for science and society. *Bull. Amer. Meteor. Soc.*, **98**, 1679–1696, <https://doi.org/10.1175/BAMS-D-15-00306.1>.
- Sorooshian, S., and Coauthors, 2011: Advanced concepts on remote sensing of precipitation at multiple scales. *Bull. Amer. Meteor. Soc.*, **92**, 1353–1357, <https://doi.org/10.1175/2011BAMS3158.1>.
- Tao, K., and P. B. Barros, 2010: Using fractal downscaling of satellite precipitation products for hydrometeorological applications. *J. Atmos. Oceanic Technol.*, **27**, 409–427, <https://doi.org/10.1175/2009JTECHA1219.1>.
- Venugopal, V., S. G. Roux, E. Foufoula-Georgiou, and A. Arneodo, 2006: Revisiting multifractality of high-resolution temporal rainfall using a wavelet-based formalism. *Water Resour. Res.*, **42**, W06D14, <https://doi.org/10.1029/2005WR004489>.
- Wang, J. X., and D. B. Wolff, 2009: Comparisons of reflectivities from the TRMM precipitation radar and ground-based radars. *J. Atmos. Oceanic Technol.*, **26**, 857–875, <https://doi.org/10.1175/2008JTECHA1175.1>.
- Warren, R. A., A. Protat, S. T. Siems, H. A. Ramsay, V. Louf, M. J. Manton, and T. A. Kane, 2018: Calibrating Ground-Based Radars against TRMM and GPM. *J. Atmos. Oceanic Technol.*, **35**, 323–346, <https://doi.org/10.1175/JTECH-D-17-0128.1>.
- Willsky, A. S., 2002: Multiresolution Markov models for signal and image processing. *Proceedings of IEEE*, **90**, 1396–1458, <https://doi.org/10.1109/JPROC.2002.800717>.
- Zhu, Y. Q., Z. H. Wang, N. Li, F. Xu, J. Han, Z. G. Chu, H. Y. Zhang, and P. C. Jiao, 2016: Consistency analysis and correction for observations from the radar at Nanjing. *Acta Meteorologica Sinica*, **74**, 298–308, <https://doi.org/10.11676/qxxb2016.022>. (in Chinese with English abstract)